Journal of Solid State Chemistry 181 (2008) 2697–2704

Contents lists available at ScienceDirect

Journal of Solid State Chemistry

journal homepage: www.elsevier.com/locate/jssc

Impact of structural features on pigment properties of α-Fe_2O_3 haematite

N. Pailhé, A. Wattiaux, M. Gaudon *, A. Demourgues

Institut de Chimie de la Matière Condensée de Bordeaux, UPR 9048 CNRS - Université de Bordeaux 1, 87 Avenue du Docteur Schweitzer, Pessac Cedex 33608, France

ARTICLE INFO

Article history:
Received 4 March 2008
Received in revised form
17 June 2008
Accepted 19 June 2008
Available online 1 July 2008

Keywords:
Red pigments
Haematite
X-ray diffraction
Mössbauer spectroscopy
Vis–NIR spectroscopy

ABSTRACT

Various α-Fe_2O_3 haematite samples were synthesized by precipitation routes (under standard or hydrothermal conditions) followed by thermal treatments under air. The trigonal distortion (C_{3v} point group) of the Fe^{3+} octahedral sites, which depends on the synthesis route and thermal treatment, was investigated by X-ray diffraction, Mössbauer spectroscopy and visible–near infrared (Vis–NIR) spectroscopy. The correlation between diffuse reflectance spectra and structural features of the haematite samples is reported and discussed herein. The slight increase of the average distortion of the Fe^{3+} octahedral sites, which depends on the annealing temperature of the precipitated sample, directly linked to the crystallite size, contrasts with the larger reduction of the sites distortion for the compound prepared by hydrothermal route due to the occurrence of hydroxyl groups substituted for O^{2-} anions as well as Fe^{3+} cationic vacancies. On a local point of view, as shown by Mössbauer spectroscopy, the Fe^{3+} octahedral sites distortion decreases from the centre towards the surface of the grains. Then the smaller the grain size, the lower the average site distortion. Finally, the reduction of the octahedral distortion was directly correlated to the two Fe–O charge transfer bands in the visible range and the colour of as-prepared haematites.

1. Introduction

α-Fe_2O_3 is an inorganic red pigment largely used for several industrial applications, for instance colouring paints, plastics and enamels, thanks to its low price, low toxicity, and high thermal and chemical stability [1,2]. Nevertheless, the dark-red colour of this mineral can strongly depend on precursors or synthesis routes [3]. In iron (III)-rich oxides such as haematite or spinels, the intense reddish-brown colour is due to an almost total absorption of the high-energy region of the visible spectrum [400–550 nm] and due to an important reflectivity in the low-energy part of the visible spectrum [550–800 nm] [4–6]. In a previous paper [7], visible–near infrared (Vis-NIR) absorption properties of haematite and spinel ferrites (AFe_2O_4) were correlated to their structural parameters. Even though numerous authors consider that all absorption bands in ferrites spinel or haematite result from Fe^{3+} 3*d* crystal field (CF) transitions [5,6,8,9], in our recent study the two main absorption edges (band-gaps) occurring in the visible range [400–800 nm] were attributed to ligand to metal $2p(O^{2-}) \rightarrow 3d(Fe^{3+})$ charge transfers. C_{3v} trigonal distortion of [FeO_6] octahedra in haematite leading to an additional *d* orbitals splitting is at the origin of this double charge transfer. Then, it seemed obvious that the octahedral sites distortion is directly linked to the energy positions of the two band-gaps as well as the two *d*–*d* intra-atomic transitions in Vis–NIR range. The aim of this work is to prepare various α-Fe_2O_3 compounds synthesized via different routes and/or with different thermal treatments and to characterize the octahedral site distortion of the various haematite compounds.

The crystal structures of these haematite samples have been studied by powder X-ay diffraction (Rietveld refinement). The local environments of the Fe^{3+} cations and the magnetic behaviour have been investigated by Mössbauer spectroscopy. Finally, the correlation of their Vis–NIR absorption spectra with their structural features will be presented.

2. Experimental details

2.1. Preparation

α-Fe_2O_3 compounds were prepared by a precipitation process in basic medium (i) or by hydrothermal route assisted by microwave (ii).

(i) A 7.2 M NH_4OH solution was added to a 0.5 M aqueous solution of iron nitrate ($Fe(NO_3)_3 \cdot 9H_2O$; Aldrich) in order to precipitate metal ions with hydroxide form $Fe(OH)_3$. According to the iron Pourbaix diagram, iron hydroxide is stable in a large pH range, from 4.5 to 10. The working pH is 9.5. The

* Corresponding author.
E-mail address: gaudon@icmcb-bordeaux.cnrs.fr (M. Gaudon).

0022-4596/$ - see front matter © 2008 Elsevier Inc. All rights reserved.
doi:10.1016/j.jssc.2008.06.049

brown precipitate was dried overnight at 100 °C. Then, in order to obtain the final α-Fe_2O_3 oxide, a thermal treatment at various temperatures (400, 600, 800 °C) for 6 h under air was performed.

(ii) The microwave-assisted synthesis was performed with a microwave digestion system (Model MARS 5, CEM Corp.) operating at a frequency of 2.45 GHz. The α-Fe_2O_3 compound was prepared from a 0.05 M $Fe(NO_3)_3 \cdot 9H_2O$ solution prepared as in the standard precipitation process (50 mL), placed in an autoclave and then treated for 2 h at 160 °C. During the process, the maximum pressure reached was about 8 bars. The precipitate powder is directly obtained with a crystallized haematite structure. The powder is just dried a few hours under primary vacuum at 100 °C.

2.2. X-ray powder diffraction

X-ray diffraction (XRD) measurements were carried out on a PANalytical X'PERT PRO diffractometer, equipped with an X-celarator detector, using Co$K\alpha$ radiation because of the fluorescence of Fe created by Cu$K\alpha$ irradiation. XRD data were recorded with 2θ steps equal to 0.017°. Diffractograms have been refined with Rietveld refinement method [10,11] using FULLPROF® software [12].

2.3. Vis–NIR diffuse reflectance measurements

The UV–Vis–NIR diffuse reflectance spectra have been obtained using a VARIAN CARY 5000 spectrophotometer equipped with an integrating sphere coated with polytetrafluoroethylene (PTFE). Measurements were performed at room temperature for wavelengths varying from 200 up to 800 nm. HALON was used as white reference. $L^*a^*b^*$ colouring space parameters of the different samples have been calculated from diffuse reflectance curves $R(\lambda)$ and from the three relative sensibility curves: $\bar{x}(\lambda)$, $\bar{y}(\lambda)$ and $\bar{z}(\lambda)$ defined by the CIE-1964. In this system, L^* is the lightness axis [black (0) to white (100)], a^* is the green (<0) to red (>0) axis, and b^* is the blue (<0) to yellow (>0) axis. Hence, stronger the a^* value, better the red pigment for industrial applications.

2.4. Mössbauer spectroscopy

^{57}Fe Mössbauer measurements were performed at 293 K on a conventional constant acceleration spectrometer (HALDER) using rhodium matrix source. As the samples contain 8 mg natural iron per cm^3, the line broadening due to thickness of samples can be neglected.

The spectrum refinement was performed in two steps. Initially, the fitting of Mössbauer patterns as a series of Lorentzian profile peaks allowed the calculation of chemical shift (δ), amplitude and width (Γ) of each peak: thus, experimental hyperfine parameters were determined for the iron octahedral site. Then, spectra analysis was made in terms of hyperfine field distribution $P(H)$ using the Hesse and Rubartsch method [13]; Γ and δ were fixed at values determined in the first refinement. This method is often used for disordered compounds with a distribution of various environments characterized by line broadening and peak shapes. This method was notably used here because of the line broadening observed for the 400 °C annealed and the hydrothermal-route compounds, leading to a peak shape differing from a Lorentzian profile and so characteristic of disordered compounds.

3. Results and discussion

3.1. Structural description

The haematite phase α-Fe_2O_3 crystallizes in hexagonal symmetry with R-3c space group related to the corundum-type structure. The Fe^{3+} iron cations are distributed with an ordering of 2/3 of the octahedral sites (12c wickoff positions) within the framework of a hexagonal close-packed array of O^{2-} ions. The crystallographic network can be described as "chains" of octahedral sites directed along the c-axis and constituted by [Fe_2O_9] dimers—two face-sharing Fe^{3+} octahedral sites—separated from each other by an empty octahedral site (Fig. 1A). Actually, the iron octahedral environment exhibits a non-centro-symmetric configuration with C_{3v} point symmetry. This trigonal distortion is induced by the strong Fe–Fe electrostatic repulsion into the face-sharing octahedral sites forming dimers. Without considering the metallic centre, the octahedral anionic cages already exhibit a C_{3v}-type distortion linked, on one hand, to the rhombohedral deformation of the unit cell (octahedral sites are flattened along the c-axis) but also because of the face-sharing octahedral site. Indeed, consequently to this configuration, only the two octahedral triangular faces perpendicular to the c-axis remain equilateral, but not equivalent: the area of the common face of two octahedra forming a dimer is smaller than that of the faces sharing an empty cationic site. At last, the cation is displaced from the geometric centre of the octahedral site along the c-axis towards the large equilateral face of the [FeO_6] octahedra forming two sets of O–Fe bond distances: three short bonds between the ligands of the large equilateral face and the metallic centre and three long bonds between the ligands of the small equilateral face and the metallic centre (Fig. 1B). Hence, the longer O–Fe bonds are associated with the strongest Fe–Fe interaction in order to relax the constraints of the network and allow optimizing the Madelung energy.

3.2. Structural study

The structural parameters of each studied compound were evaluated by powder XRD. Whatever the synthesis route, a pure phase has been obtained with the corundum-type structure. The Rietveld refinement plots (experimental, theory and difference) of the "precipitated route haematites" obtained after heat treatment at 400 and 800 °C as well as the "hydrothermal route haematite" are presented in Figs. 2a–c, respectively, as illustration. Refined parameters, i.e. cell parameters, atomic positions, occupancies as

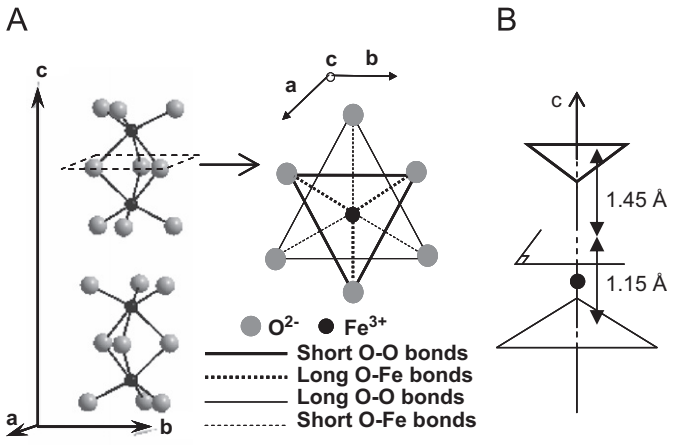

Fig. 1. Structural representations of haematite: chains of [FeO_6] dimers along the c-axis (A) in corundum structure. Illustration of the "small" and the "large" equilateral triangles and the Fe^{3+} displacement from the octahedral site centre (B).

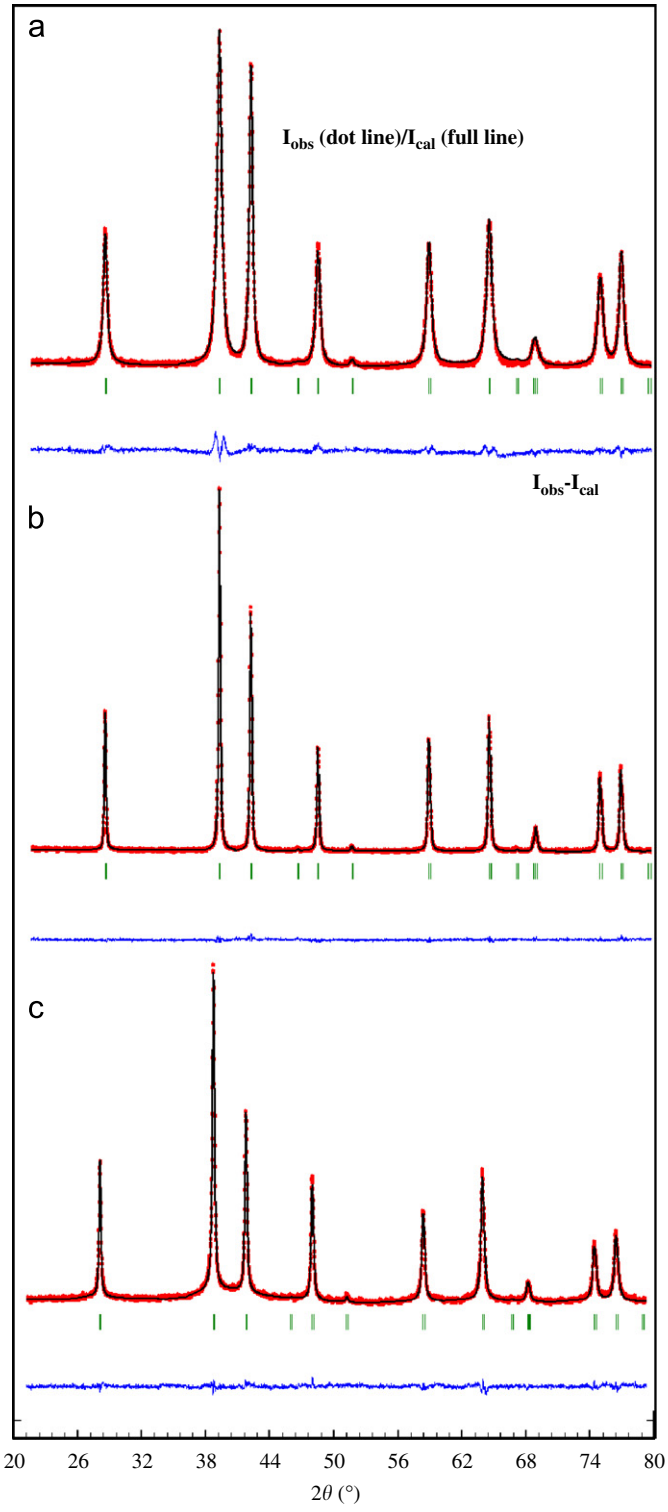

Fig. 2. Rietveld refinement plot of 400 °C fired (a), 800 °C annealed samples (b) and hydrothermal-route sample (c). The lowest line is the difference between the calculated and experimental data. Source: Co($K\alpha_1$/$K\alpha_2$).

well as reliability factors, are reported in Table 1 for a commercial haematite (Aldrich-99+%-n°31,005-0) as well as for all prepared compounds, i.e. precipitated route haematites, annealed at 400, 600 and 800 °C, and the hydrothermal route haematite. The refinement performed on the commercial powder with fixed occupancies allowed obtaining the isotropic displacement factors (Debye–Waller factors: B); then fixed B(Å^2), 0.35 Å^2 for Fe^{3+} and 0.74 Å^2 for O^{2-}, were considered in the case of as-prepared compounds. Coherent domains were evaluated with Sherrer formula from the integral width of the diffraction patterns' peaks, taking into account the instrument width. It appears that the crystallite size of each compound is clearly larger than the Bohr radius of semi-conductors (~5 nm). Therefore, no quantum confinement can be considered, and so diffuse reflectance curves can be directly related to the corundum-type structure. Moreover, O–Fe and O–O (corresponding to large and small equilateral triangles) bond distances were compiled from the different structure refinements and are reported in Table 2.

Firstly, the refinement results of the different precipitated route α-Fe_2O_3 are discussed. Satisfactory reliability factor values have been obtained (R_B~3.3%) except in the case of the 400 °C-annealed compound ($R_{Bragg}>6$), where the anisotropy of particles have to be taken into account and has been described, in more detail, in a forthcoming paper [14]. Iron occupancies are near to 100% for all the compositions annealed at 400, 600 and 800 °C, showing that Fe^{3+} ion sites (12c) are fully occupied. No traces of hydroxyl OH^- groups have been considered in the structure. In each case, refinements resulted in two different bond distances O–Fe (~2.12 and ~1.94 Å) and two different O–O bond distances associated to the equilateral triangles, reported in Table 2, as a consequence of the C_{3v}-type distortion. Finally, a more flattened octahedral site corresponds to one larger and one smaller equilateral face and an important iron displacement. Thus, the octahedral distortion was deduced hereafter from the iron and oxygen atomic positions, the octahedron [FeO_6] being all the more regular as the atomic positions (x_O and z_{Fe}) are close to 1/3. According to atomic position values reported in Table 1 and illustrated in Fig. 3 (despite the high value of standard deviations of x_O and z_{Fe} coordinates for the 400 °C-annealed compound), one can notice in first approximation that the octahedral site distortion seems directly linked to the crystallite size, which is directly governed by the temperature of the thermal treatment. The lower the annealing temperature, the lower the distortion of the octahedral sites because of decrease in the atomic positions, x_o and x_{Fe}. It can be concluded that the crystallite size governs the structural parameters of the haematites obtained from the precipitation route. It can be supposed that a low annealing temperature related to small crystallite size does not allow reaching the stable configuration with the higher Madelung energy. This point will be discussed in the next section related to Mössbauer investigations.

Secondly, for the hydrothermal route sample, the c-cell parameter (13.8024(6) Å) and x-oxygen position (0.3128(7)) values are particularly high, whereas the Fe occupancy seems to be different and lower than 1 (0.883(6)) compared to the precipitated route compounds or literature data [15,16]. In this case, the iron occupancy value corresponds approximately to 0.9. It seems obvious that this haematite compound exhibits an iron non-stoichiometry, with OH^- groups substituting for O^{2-} ions. In literature [17,18], it was shown by FTIR investigations that hydroxyl groups OH^- can still be present in the haematite structure until 1000 °C. OH^- ions would occupy anionic positions in the hexagonal close-packed anionic sub-lattice of haematite. In order to keep the electroneutrality, Fe^{3+} vacancies would be stabilized into the network. Consequently, the formula of hydroxyl-haematite could be written as $Fe_{2-x/3}\kappa_{x/3}(OH)_xO_{3-x}$. According to the refinement results, the formula of this hydrothermal-route compound would be roughly $Fe_{1.8}(OH)_{0.6}O_{2.4}$. A thermogravimetric analysis was performed, an effective weight loss being recorded. The two successive losses at about 140 °C and from 210 to 450 °C show the occurrence of adsorbed water and bulk OH^- hydroxyl groups, respectively. Although these weight losses could not be accurately quantified because of the strong convolution of the two phenomena, bulk OH^- groups have been

Table 1
Rietveld refinement results of the precipitated (400, 600, 800 °C), hydrothermal route and commercial α-Fe_2O_3

Atom	Site	x	y	z	Biso	Occupancy
400 °C						
α-Fe_2O_3 (R-3c)	*Crystallite size = 17(5) nm*					
a = 5.03459(31) Å, c = 13.7533(13) Å	*R_p = 2.27%*			*Rw_p = 2.97%*		*R_{Bragg} = 6.72%*
Fe1	12*c*	0	0	0.35496(25)	0.35	0.991(15)
O	18*e*	0.3088 (17)	0	$\frac{1}{4}$	0.74	1
Score = 6.2809 (Berar's formula)						
600 °C						
α-Fe_2O_3 (R-3c)	*Crystallite size = 31(6) nm*					
a = 5.03506(6) Å, c = 13.75053(20) Å	*R_p = 1.82%*			*Rw_p = 2.30%*		*R_{Bragg} = 3.31%*
Fe1	12*c*	0	0	0.35520(4)	0.35	0.994(3)
O	18*e*	0.3069(3)	0	$\frac{1}{4}$	0.74	1
Score = 1.9586 (Berar's formula)						
800 °C						
α-Fe_2O_3 (R-3c)	*Crystallite size = 58(5) nm*					
a = 5.03594(5) Å, c = 13.74439(15) Å	*R_p = 2.01%*			*Rw_p = 2.57%*		*R_{Bragg} = 3.26%*
Fe1	12*c*	0	0	0.35528(5)	0.35	1
O	18*e*	0.3071(3)	0	$\frac{1}{4}$	0.74	1
Score = 1.6359 (Berar's formula)						
Hydrothermal						
α-Fe_2O_3 (R-3c)	*Crystallite size = 72(5) nm*					
a = 5.03576(17) Å, c = 13.80238(58) Å	*R_p = 1.72%*			*Rw_p = 2.20%*		*R_{Bragg} = 5.52%*
Fe1	12*c*	0	0	0.35408(12)	0.35	0.883(6)
O	18*e*	0.3127(7)	0	$\frac{1}{4}$	0.74	1
Score = 2.4150 (Berar's formula)						
Commercial						
Fe_2O_3 (R-3c)	*Crystallite size = 155(5) nm*					
a = 5.03582(5) Å, c = 13.75026(12) Å	*R_p = 3.03%*			*Rw_p = 3.90%*		*R_{Bragg} = 3.19%*
Fe1	12*c*	0	0	0.35537(7)	0.35(4)	1
O	18*e*	0.3073(6)	0	$\frac{1}{4}$	0.74(8)	1
Score = 2.4220 (Berar's formula)						

Table 2
Average oxygen–iron and oxygen–oxygen distances in hematites α-Fe_2O_3

Compound	400 °C	600 °C	800 °C	Hydrothermal	Commercial
O–Fe (Å)	2.122(8)	2.117(4)	2.118 (3)	2.132 (4)	2.120 (4)
	1.939(4)	1.942(2)	1.941 (1)	1.936 (2)	1.941 (2)
O–O (Å)	3.023(8)	3.029(5)	3.028(5)	3.001(8)	3.027(5)
	2.686(8)	2.677(5)	2.679(5)	2.728(8)	2.680(5)

O–O: edge distances of the two equilateral triangles.

graphically estimated at about 4 wt%, a value close to the one calculated from XRD analysis (~4.5 wt%).

The expansion of the unit cell in *c*-direction (13.8024(6) Å instead of 13.7505(2) Å) could be explained by the important content of hydroxyl group; indeed, the equilibrium Fe–OH bond length, with OH^- located in tetrahedral coordination, can be calculated from valence bond calculation following Brown and Altermatt law [19]: the calculated value is about 2.27 Å. This bond is so significantly longer than the higher O–Fe bond distance in haematite (around 2.12 Å). Then the expansion of the unit cell occurs along the *c*-axis and not along the *a*/*b*-axes, showing the relaxation of the octahedra along the *c*-axis is due to the limitation of Fe–Fe interactions and the presence of H^+. Thus, the compound prepared by hydrothermal route is the only case where the *c*-parameter is higher than $a(\sqrt{3}+1)$ equilibrium value and the octahedral sites are elongated along the *c*-axis. The consequence of the octahedral site elongation is that Fe^{3+} cations relax along the *c*-axis. The z_{Fe} coordinate decreases whereas the x_O coordinate increases, both these values tending towards the equilibrium value, equal to 1/3. It shows that the area of the small triangle face increases whereas the area of the large ones decreases.

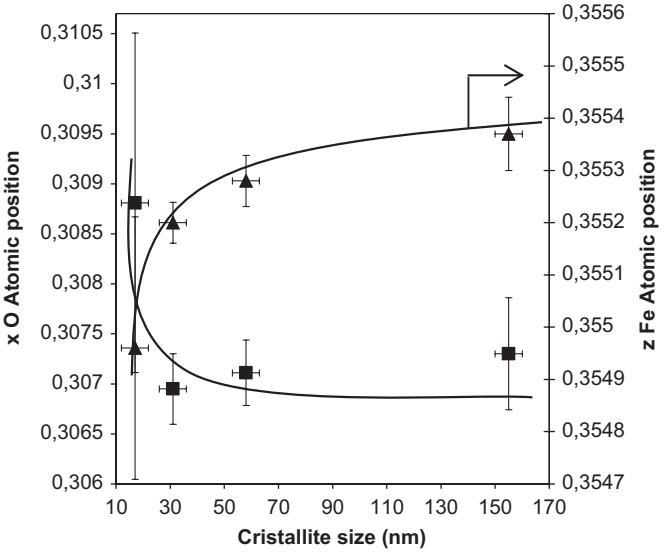

Fig. 3. Illustration of the correlation between the particle diameter of precipitated and commercial haematites and atomic positions relative to the octahedral site distortion.

3.3. Mössbauer spectroscopy

^{57}Fe Mössbauer measurements were carried out on the precipitated compounds and on the commercial haematite in order to follow the local environment of Fe^{3+} iron versus particle size. Experimental and calculated spectra for 400 and 800 °C

annealed samples are reported in Fig. 4. The good refinement of each Mössbauer spectrum demonstrates the purity of the samples: no traces of Fe^{2+} were detected. The experimental spectra of the compounds exhibit a perfect sextuplet, the signature of a magnetically ordered compound (anti-ferromagnetic ordering) as referred in literature [20,21]. However, there is a notable line broadening of spectra for the 400 and 600 °C annealed compounds, indicating a magnetic disorder associated to various distortions of iron octahedral sites. The hyperfine parameters of each compound are collected in Table 3. The hyperfine field distributions of the compounds annealed at 400, 600 and 800 °C are reported in Fig. 5. Considering the shape of the three curves, it is obvious that the hyperfine field distribution width is broader when the annealing temperature is low. The average magnetic field and field width could then be extracted using a Newman integration of the hyperfine field distribution. The average field ($H_{50\%}$ or $\bar{H}$) corresponds to the value which divides the area under the curve into two equal parts. Here, the inverse of the hyperfine field distribution width (ΔH^{-1}) corresponding to $(H_{60\%}-H_{40\%})^{-1}$ give a significant representation of the sharpness of the signal by neglecting its residual or parasitical parts. Hence, from the field distribution and crystallite size evaluation deduced from XRD data refinement, the variations of the hyperfine field $\bar{H}$ and ΔH^{-1} versus the crystallite diameter of each sample are both plotted in Fig. 6a. The two evolutions exhibit a similar asymptotic shape versus crystallite size. The very low value of ΔH^{-1}, corresponding to the smallest crystallite, is related to high iron site heterogeneity for the 400 °C annealed sample, as mentioned previously. Small crystallites reveal a large surface area associated with a large surface/bulk atomic ratio. The variation of the atomic percentage in the bulk as a function of crystallite size is represented in Fig. 6b. The calculation of the atomic rate in the bulk was performed by assuming the crystallite as spheres. Thus, bulk atoms rate is proportional to $100^*(1-K/r)$, with r the crystallite radius in Å and K being a constant. The asymptotic shape of the curve, similar to the one observed in Fig. 6a, allows to correlate $\bar{H}$ and ΔH^{-1} to the atomic concentration in the bulk. Thus, a compound with 100% bulk atoms as a perfect crystal could be associated to a Dirac field distribution (ΔH^{-1} tends to an asymptotic value corresponding to a Gaussian field distribution related to the instrumental resolution), with an asymptotic value of the average field curve equal to 51.8 T. On the contrary, the occurrence of a large atomic content at the surface induces a decrease of $\bar{H}$ and ΔH^{-1} values. An interpretation of these phenomena can be proposed: the haematite crystallites exhibit an H gradient from bulk towards the surface corresponding to an H decrease. One can compare this with the XRD data refinements showing a global reduction of the octahedral site distortion versus decreasing particle size. Actually, haematite particles seem to exhibit a gradient of octahedral sites distortion from bulk towards surface, the less distorted octahedral sites moving closer to $[O_h]$ symmetry. Indeed, the octahedral distortion being due to face-sharing octahedral sites forming dimers, one can assume that during the crystallite germination and growth (i.e. during the space extension of the corundum-type network), an all the more important octahedral distortion occurs.

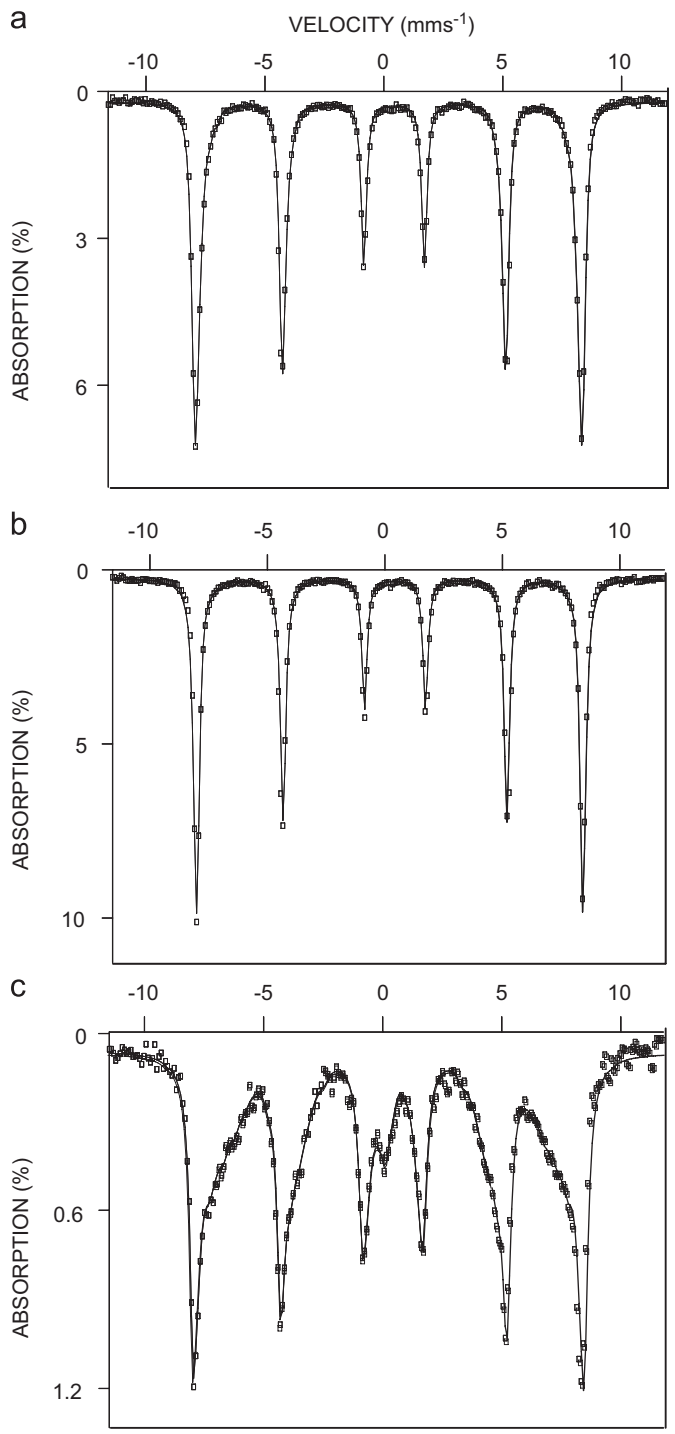

Fig. 4. Room temperature Mössbauer spectra of α-Fe_2O_3—400 °C (a), 800 °C (b) annealed samples and hydrothermal-route sample (c). The calculated spectrum is represented by the full line.

^{57}Fe Mössbauer measurements were also performed on the hydrothermal-route compound. Experimental and calculated spectra are reported in Fig. 4, while hyperfine parameters are collected in Table 3. The very broad hyperfine field distribution width is clearly characteristic of the presence of heterogeneous octahedral sites. Part of the Fe^{3+} ions were considered as regular sites of corundum network because of their peak profile parameters ($\delta = 0.36$ mm/s, $\Gamma = 0.3$ mm/s, $\bar{H}\sim 50$ T). Considering two iron populations, Fe^{3+} in corundum structure and all the other irons inserted in more or less distorted octahedra, the corundum-type irons are estimated to be about 26% of the population. Therefore, for the hydrothermal-route compound corresponding to a hydroxyl-haematite, it can be assumed that this last population would represent $[FeO_6]$ octahedral sites while the other octahedral sites would combine the two types of ligands, OH^- and O^{2-}, and so would have a distortion degree intermediate between the two $[FeOH_6]$ and $[FeO_6]$ extreme sites. The probability to find a Fe^{3+} cation linked to six O^{2-} ligands was calculated, from a binomial law applied with the OH^- and O^{2-} occupancies determined from XRD and TGA measurements.

Table 3
Hyperfine parameters deduced from Mössbauer spectroscopy of hematite compounds

Compound	Distribution	δ (mm/s)	Γ (mm/s)	ε (mm/s)	Δ^* (mm/s)	H^* (T)	(%)	Iron site
Commercial α-Fe_2O_3	1	0.37	0.25	(−)0.115	–	51.6	100	Fe3+ [Oh]
α-Fe_2O_3 800 °C	1	0.36	0.25	(−)0.113	–	51.4	100	Fe3+ [Oh]
α-Fe_2O_3 600 °C	1	0.37	0.25	(−)0.113	–	51.1	100	Fe3+ [Oh]
α-Fe_2O_3 400 °C	1	0.37	0.25	(−)0.113	–	50.3	100	Fe3+ [Oh]
α-Fe_2O_3 160 °C (hydrothermal)	1	0.36	0.30	(−)0.110	–	49.5	26	Fe3+ [Oh]
	2	0.38	0.50	(−)0.100	–	45.0	65	Fe3+ [Oh]
	3	0.15	0.40	–	0.44	–	9	Fe3+ [Oh]

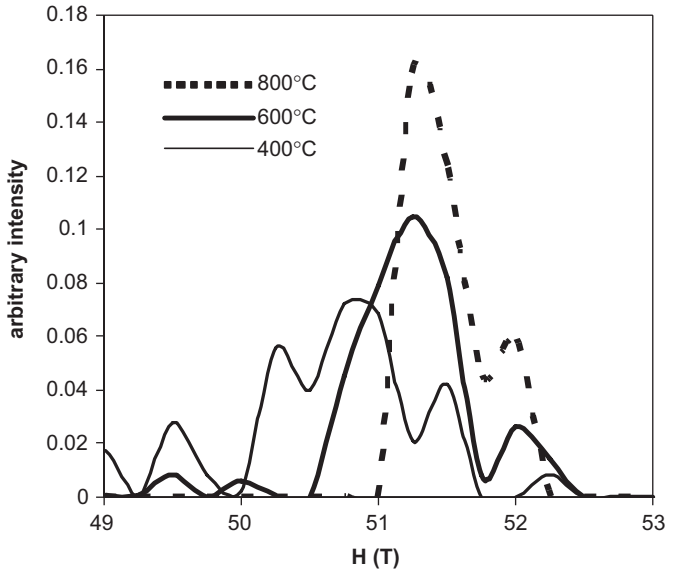

Fig. 5. Hyperfine field distributions of precipitated haematites annealed at various temperatures.

It led to a relative coherent value around 20%, compared to the refined one from the Mössbauer spectrum equal to 26%.

3.4. Diffuse reflectance study

Diffuse reflectance curves measured in the Vis–NIR range for all haematite compounds are presented in Fig. 7, while enlargement of the associated derivative curves in the visible region is shown in Fig. 8.

As expected, whatever the annealing temperature or synthesis route, the two main absorption edges, noted CT_1 (~2 eV) and CT_2 (~1.7 eV) correspond to two possible anion-to-cation charge transfers from 2*p*-orbitals of oxygen O^{2-} to 3*d*-orbitals of Fe^{3+} cations in C_{3v} symmetry and occur in the visible range, as mentioned in previous papers [4,7]. Moreover, on the basis of the Tanabe–Sugano diagram, corresponding to [O_h] symmetry, the absorption band centred at about 860 nm (Fig. 8) is related to the *d*–*d* intra-atomic transition $^6A_{1g} \rightarrow {}^4T_{1g}$, while the *d*–*d* intra-atomic transition $^6A_{1g} \rightarrow {}^4T_{2g}$ should appear at about 640 nm, both these transitions being associated to a 10 Dq CF equal to 1.5 eV [7]. Indeed, spin-forbidden CF transitions become spin-allowed by magnetic interactions occurring in such compounds [6]. ΔE values, equal to the difference in energy (eV) between the two band-gap positions ($\Delta E = CT_1 - CT_2$), are reported in Table 3 for each studied compound. For the precipitated compounds series, the CT_1 and CT_2 bands are all the more separated as the annealing temperature is high. In order to correlate the octahedral sites distortion versus optical properties, atomic coordinates of Fe and O atoms versus ΔE have been plotted in Fig. 9. Moreover, one can notice in Fig. 10 that the energy difference between the two charge transfer bands is smaller as atomic positions (x_O as well as z_{Fe}) get closer to 1/3, hence shifting from C_{3v} to O_h symmetry. Finally, the hydrothermal-route compound exhibits interesting properties radically different from those of precipitated-route compounds, because of the lowest energy difference between CT_1 and CT_2. This is clearly due to an effect of the octahedral sites distortion previously underlined: the smaller average distortion of the octahedral sites of this compound compared to the precipitated-route or commercial haematite explains the evolution of the energy position of the two charge transfer bands. Furthermore, the slight shift at high energy of the $^6A_{1g} \rightarrow {}^4T_{1g}$ *d*–*d* transitions (850 nm instead of 860 nm) is consistent with the reduction of the CF as predicted by the Tanabe–Sugano diagram. This CF decrease is due to the OH^- anions' partial substitution for O^{2-} ones.

In all cases, ΔE is directly related to the distortion degree of the octahedral sites in the corundum structure. Indeed, this correlation still exists whatever the driving force of the octahedral site distortion associated to low annealing temperature as well as the occurrence of hydroxyl groups and Fe vacancies inside the corundum framework. This study confirms the hypothesis advanced in a previous paper [7]: C_{3v}-type distortion of [FeO_6] octahedra in haematite is at the origin of the double charge transfer because of the additional Fe^{3+} t_{2g}-orbitals splitting induced by the CF. Then, ΔE increases with the distortion degree of the octahedral sites because the t_{2g} splitting increases as the Fe^{3+} sites move from O_h to D_{3d} and C_{3v} symmetries. Moreover, the variation of the structural parameter strongly contributes to modify the colour of the haematite. The $L^*a^*b^*$ space parameters relative to the precipitated and the hydrothermal compounds are reported in Table 4. The higher a^* values in the case of the 400 °C annealed haematite and the hydrothermal compound contribute to the more reddish colour of these samples. Consequently, in the haematite framework, the closer the Fe^{3+} site to the O_h symmetry, the more pronounced red is the coloration of the haematite (Table 5).

4. Conclusion

Depending on the synthesis conditions, the composition and/or crystallite size of haematites were controlled, allowing to tune the trigonal distortion of the Fe^{3+} octahedral sites and so the colour of the obtained samples. Indeed, the evolution of the trigonal distortion directly influences the crystal field intensity and splitting, and so the energy positions of the charge transfer bands as well as the *d*–*d* absorption bands located in the visible–NIR range. It is an outstanding example where the crystallite size, even far out of the quantum confinement scale, allows controlling the intrinsic coloration of a compound. Here, it was shown that the haematite colour is particularly dependent on the convolution (ΔE) of the two charge transfer bands occurring at about 2.1 and 1.75 eV: the smaller the crystallite size, the lower

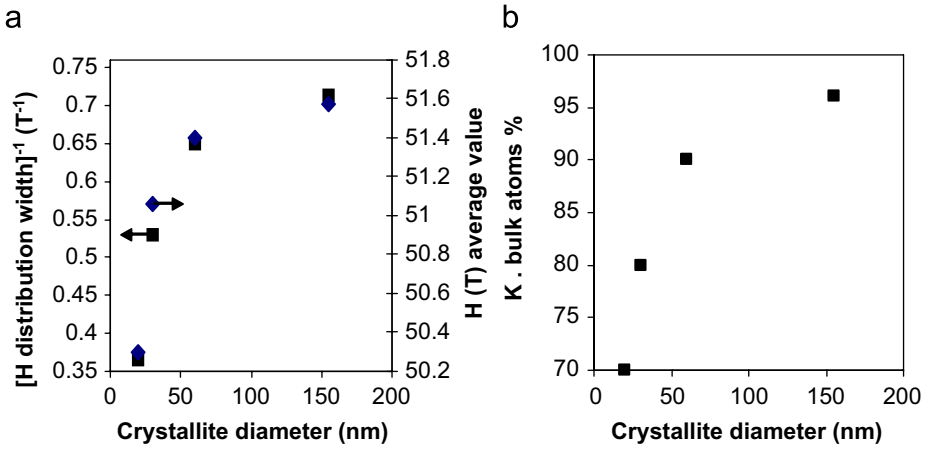

Fig. 6. Evolution of hyperfine average field $\bar{H}$ and ΔH^{-1} (a), and bulk atoms amount (b) versus particle size of precipitated haematites.

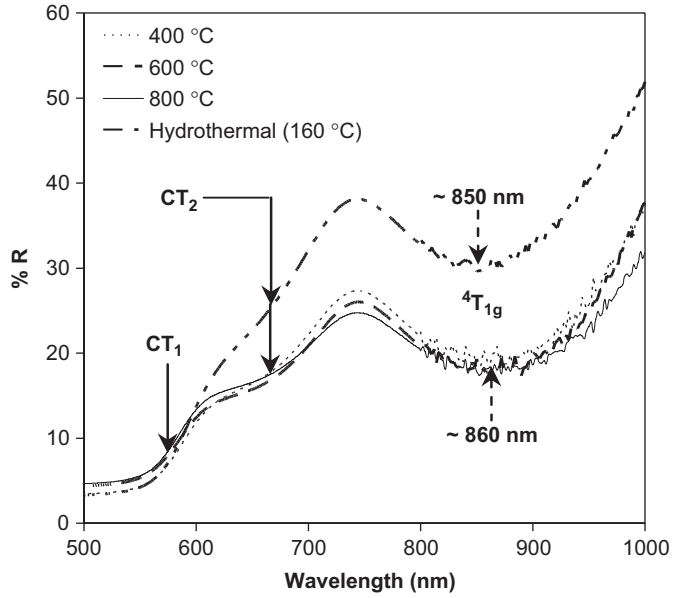

Fig. 7. Diffuse reflectance spectra of haematite compounds. CT_1 and CT_2 represent the $O(2p) \rightarrow Fe(3d)$ charge transfers in $[FeO_6]$ distorted octahedron.

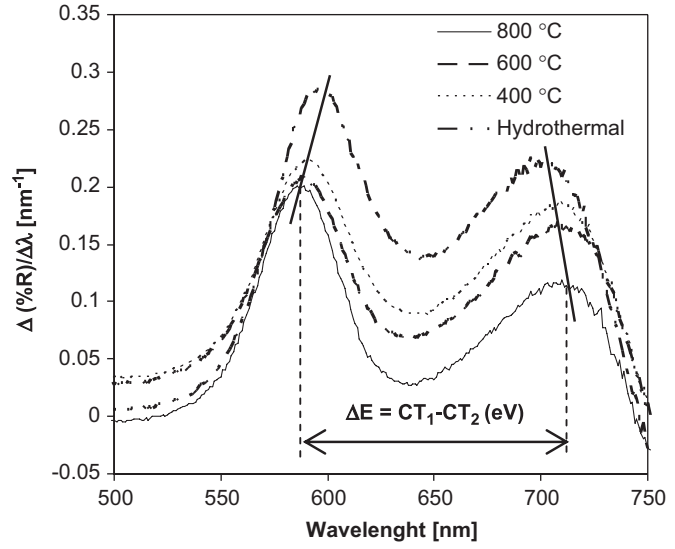

Fig. 8. Derivative curves from diffuse reflectance spectra of haematite compounds.

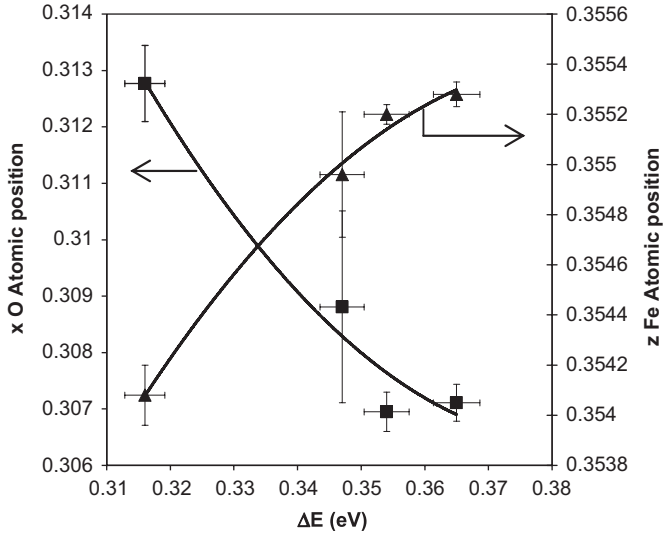

Fig. 9. Illustration of the correlation between the optical properties and the octahedral site distortion followed from Fe, O atomic positions.

Table 4
ΔE values measured from derivative curves of diffuse reflectance spectra of each compound

	Hydrothermal (160 °C)	400 °C	600 °C	800 °C
ΔE (eV)	0.316 (3)	0.347 (3)	0.354 (3)	0.365 (4)

Table 5
Trichromatic coordinates $L^*a^*b^*$

Sample	L^*	a^*	b^*
400 °C	30.4	21.4	19.5
600 °C	32.5	18.3	16.1
800 °C	35.0	18.7	17.5
Hydrothermal	34.1	27.0	23.6

the average octahedral distortion, and the more saturated the red coloration of the synthesized haematites. One fundamental question remains still open: is it possible to move down the ΔE energy difference until finally obtaining only one $O^{2-} \rightarrow Fe^{3+}$ charge transfer band for the haematite framework or related structures? It seems indeed difficult to obtain non-distorted Fe^{3+} octahedral sites. Nevertheless, thanks to the correlation between

composition, structural features and electronic transitions in Vis–NIR regions, this study opens the possibility to develop new iron-based pigments as well as NIR absorbers with various band-gaps, interesting for photovoltaic applications.

References

[1] A.L. Peter, Pigment Handbook, Wiley, New York, USA, 1987.
[2] R.M. Cornell, U. Schwertman, The Iron Oxides: Properties, Reactions, Occurrence, and Uses, Weinheim, VCH, New York, 1996, pp. 1–25.
[3] H. Katsuki, S. Komarneni, J. Am. Ceram. Soc. 86 (1) (2003) 183–185;
L. Dengxin, G. Guolong, M. Fanling, J. Chong, J. Hazard. Mater. 155 (1–2) (2008) 369–377;
K.J. Sreeram, R. Indumathy, A. Rajaram, B.U. Nair, T. Ramasami, Mater. Res. Bull. 41 (10) (2006) 1875–1881
J. Hazard. Mater. 155(1–2) (2008) 369–377.
[4] M. Elias, C. Chartier, G. Prévot, H. Garay, C. Vignaud, Mater. Sci. Eng. B 127 (2006) 70–80.
[5] C.S. Kosmas, D.P. Franzmeier, D.G. Schulz, Clays Clay Miner. 34 (6) (1986) 625–634.
[6] G.R. Rossman, in: M.D. Dyar, C. McCammon, M.W. Schaefer (Eds.), The Geochemical Society, Special Publication No. 5, 1996, pp. 23–27.
[7] N. Pailhé, A. Wattiaux, M. Gaudon, A. Demourgues, J. Solid State Chem. 181 (5) (2008) 1040–1047.
[8] D.M. Shermann, T.D. Waite, Am. Miner. 70 (1985) 1262–1269.
[9] J. Torrent, V. Barron, Clays Clay Miner. 51 (3) (2003) 309–317.
[10] H.M. Rietveld, Acta Crystallogr. 22 (1967) 151–152.
[11] H.M. Rietveld, J. Appl. Crystallogr. 2 (1969) 65–71.
[12] J. Rodriguez-Carvajal, in: Abstracts of the Satellite Meeting on Powder Diffraction of the XV Congress of the IUCr, Toulouse, France, 1997, pp. 127–135.
[13] J. Hesse, A. Rubartsch, J. Phys. E Sci. Instrum. 7 (1974) 526.
[14] N. Pailhé, S. Pechev, M. Gaudon J. Majimel, A. Demourgues, J. Appl. Crystallogr. (2007), submitted.
[15] V.G. Tsirel'son, et al., Dokl. Akad. Nauk SSSR 298 (1988) 1137.
[16] E.N. Maslen, et al., Acta Crystallogr. B 50 (1994) 435–441.
[17] E. Wolska, Monatsh. Chem. 108 (1977) 819–828.
[18] E. Wolska, Zeitschr. Kristallogr. 154 (1981) 69–75.
[19] I.D. Brown, D. Altermatt, Acta Crystallogr. B 41 (1985) 244–247.
[20] F.J. Morin, Phys. Rev. 83 (1951) 1005.
[21] F.J. Berry, C. Greaves, Ö. Helgason, J. McManus, H.M. Palmer, R.T. Williams, J. Solid State Chem. 151 (2000) 157–162.